Check for updates

Nanostructured carbons containing FeNi/NiFe$_2$O$_4$ supported over N-doped carbon nanofibers for oxygen reduction and evolution reactions†

Iram Aziz,[a] JinGoo Lee, [ID][b] Hatice Duran, [ID][c] Katrin Kirchhoff,[d] Richard T. Baker, [ID][b] John T. S. Irvine [ID][b] and Salman N. Arshad [ID]*[a]

Non-precious metal-based electrocatalysts on carbon materials with high durability and low cost have been developed to ameliorate the oxygen-reduction reaction (ORR) and oxygen-evolution reaction (OER) for electrochemical energy applications such as in fuel cells and water electrolysis. Herein, two different morphologies of FeNi/NiFe$_2$O$_4$ supported over hierarchical N-doped carbons were achieved *via* carbonization of the polymer nanofibers by controlling the ratio of metal salts to melamine: a mixture of carbon nanotubes (CNTs) and graphene nanotubes (GNTs) supported over carbon nanofibers (CNFs) with spherical FeNi encapsulated at the tips (G/CNT@NCNF, 1 : 3), and graphene sheets wrapped CNFs with embedded needle-like FeNi (GS@NCNF, 2 : 3). G/CNT@NCNF shows excellent ORR activity (on-set potential: 0.948 V *vs.* RHE) and methanol tolerance, whilst GS@NCNF exhibited significantly lower over-potential of only 230 mV at 10 mA cm^{-2} for OER. Such high activities are due to the synergistic effects of bimetallic NPs encapsulated at CNT tips and N-doped carbons with unique hierarchical structures and the desired defects.
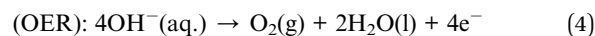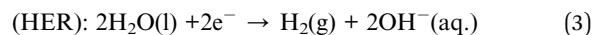
1. Introduction

The ever-increasing energy demand has shifted the focus from fossil fuels to cleaner, renewable, and sustainable resources, which has stimulated the development of hydrogen-based energy systems.[1,2] Fuel/electrolysis cells have been considered as a promising technology because not only do they generate electricity from hydrogen fuels in fuel cell mode, but they can also produce hydrogen from water in the electrolysis mode. These are based on hydrogen oxidation reaction (HOR) and oxygen reduction reaction (ORR) for fuel cells and hydrogen evolution reaction (HER) and oxygen evolution reaction (OER) for electrolysis cells.[3] The reaction mechanisms in alkaline solution are given below.

Fuel cell mode:

$$(HOR): H_2(g) + 2OH^-(aq.) \rightarrow 2H_2O(l) + 2e^- \qquad (1)$$

[a]Department of Chemistry and Chemical Engineering, Syed Babar Ali School of Science and Engineering, Lahore University of Management Sciences, Lahore 54792, Pakistan. E-mail: salman.arshad@lums.edu.pk; Tel: +92-42-35608478

[b]EaStChem, School of Chemistry, University of St. Andrews, North Haugh, St Andrews, Fife, KY16 9ST, UK

[c]Department of Materials Science and Nanotechnology Engineering, TOBB University of Economics and Technology, Ankara, Turkey

[d]Max-Planck-Institute for Polymer Research, Ackermannweg 10, 55128 Mainz, Rhineland-Palatinate, Germany

† Electronic supplementary information (ESI) available. See DOI: 10.1039/c9ra08053h

$$(ORR): O_2(g) + 2H_2O(l) + 4e^- \rightarrow 4OH^-(aq.) \qquad (2)$$

Electrolysis mode:

$$(HER): 2H_2O(l) + 2e^- \rightarrow H_2(g) + 2OH^-(aq.) \qquad (3)$$

$$(OER): 4OH^-(aq.) \rightarrow O_2(g) + 2H_2O(l) + 4e^- \qquad (4)$$

ORR and OER are both four electron transfer processes requiring high driving potentials and their sluggish kinetics limits the overall performance.[4] Noble metal based catalysts like Pt/C for ORR/HER and RuO$_2$/IrO$_2$ for OER are considered as the benchmark catalysts because of their self-standing structure, hydrophilicity, specific surface area and unique morphology (nanotubes, core–shell structure *etc.*).[5–7] However, high costs and low durability during long-term use inhibits their practical use. Another limitation is that these catalysts show outstanding performance predominantly for one type of reaction. For example, Pt/C is excellent catalyst for ORR but it shows poor kinetics for OER because of the formation of an inactive oxide film on Pt/C.[8,9] Thus, there is a dire need to design a robust, bifunctional, and non-noble metal based catalysts.[10,11] Many efforts have been made to replace the precious metal catalysts with non-precious metals supported over carbonaceous materials for improved efficiency, selectivity and stability.[12] Doping of heteroatom (N, P, B and S) in carbon based structures like CNTs,[13] CNFs,[14] carbon nanosheets[15] and graphene[16] can break the electro-neutrality of the carbon and yield active sites for the

electrochemical reaction. Gong *et al.*[17] prepared vertically aligned CNT arrays which showed superior performance for ORR compared to Pt/C when doped with N due to the high positive charge density. Moreover, co-decoration of metals (Fe, Co and Ni) on N-doped carbon resulted in synergistic enhancement in the bifunctional activity.[18] The exact mechanism is still not well understood, however, it is assumed that the metal forms a chelate M–N$_4$ which act as an active site with a high M$^{2+/3+}$ redox potential.[19,20]

CNTs supported over CNFs show promising ORR activity due to high pyridinic-N content where CNFs also provide an excellent support due to its high electrical conductivity, thermal stability and flexibility.[21] Although active sites can be easily introduced on CNFs due to the presence of disorders which facilitates the adsorption of oxygen,[22] the large contact resistance and restricted charge transfer hinders their performance.[23] CNTs, on the other hand, offers good electrical conductivity and chemical stability.[24] Thus, hybrids of CNTs and CNFs (*e.g.* synthesized by growth of CNTs over CNFs) can potentially offer more active sites with higher electrical conductivity and stability for enhanced activity in electrocatalysis.[25] Typically, metal based N-doped CNTs are grown on a substrate using chemical vapor deposition (CVD),[26] however, it cannot be easily separated and transferred to another substrate such as CNFs. This can be overcome by direct growth of CNTs on the surfaces of electrospun CNF by CVD using metal loaded polymer NFs as precursor.[27] Such hybrid structures exhibit strong and seamless interconnection between the active material and electrode to deliver enhanced electrocatalytic activity.[28,29] Such carbon based hybrid structures can also be grown using bimetallic alloy NPs which themselves have better electrocatalytic activity compared to single metal because of the enhanced stability of higher oxidation states in one metal[30] and better charge transfer driven by greater intrinsic polarity.[31] To this end, FeNi is recognized as an excellent catalyst for both ORR and OER.[32] Chuangang *et al.*[33] prepared carbon capsules with N-doped CNT whiskers on the surface by loading Fe and Ni metal which exhibited very high specific surface area of ~985 m^2 g^{-1} and a superior ORR activity than Pt/C with half-wave potential of 0.88 V (*vs.* RHE). Gupta *et al.*[34] prepared graphene nanotubes (GNTs), with thin walls and diameter ~500 nm, using binary and ternary metal alloys (FeNi, FeCo, NiCo and FeNiCo) as catalysts and dicyandiamide as precursor. These bifunctional catalysts showed superior catalytic activity for both OER and ORR. Unni *et al.*[35] prepared Fe$_3$O$_4$ encapsulated GNTs with a surface area of 750 m^2 g^{-1} from single-walled CNTs which showed enhanced ORR performance in both acidic and alkaline media. Wang *et al.* synthesized FeNi NPs embedded electrospun CNFs which showed best activity for Fe : Ni ratio of 1 : 1 with an onset potential of 0.903 V and 1.528 V for ORR and OER, respectively, with charge transfer resistance of 48.1 Ω.[36]

Thus, designing a low cost and scalable process for *in situ* growth of hierarchical carbon nanostructures with adequate N-doping and loaded with metal alloy/oxide NPs will be very promising. Herein, *in situ* growth of CNTs, GNTs, and graphene sheets (GS) supported over N-doped CNFs is reported as a potential one-pot synthesis method. Two distinct type of hierarchical structures were formed depending on the ratio of nitrogen-rich melamine to metal salt precursors; (i) needle-like FeNi embedded graphene sheets which were wrapped over CNFs, and (ii) bamboo-shaped CNTs and GNTs over CNF surfaces with spherical FeNi at tips. Both these samples showed very promising electrocatalytic activity for ORR and OER which signifies the potential of this facile method to fabricate hierarchical and functional carbon nanomaterials.

2. Experimental procedures

2.1. Material synthesis

Polyacrylonitrile (PAN, M_n ≈ 150 000 g mol^{-1}), *N,N*-dimethylformamide (DMF), iron(III) chloride hexahydrate (FeCl$_3$·6H$_2$O), nickel(II) chloride hexahydrate (NiCl$_2$·6H$_2$O) and Nafion perfluorinated resin solution (5 wt%) were purchased from Sigma-Aldrich. Melamine and 40% Pt/C (HiSPEC 4000) was purchased from Alfa Aesar and KOH from Fischer Chemical. First, 900 mg of PAN was dissolved in 10 mL of DMF by overnight stirring to form an electrospinning solution which was electrospun at 20 kV with a needle-to-collector distance of 20 cm. The resulting NFs were stabilized in air at 250 °C for 2 h and then stirred for 30 min with melamine in DMF. After filtering, the melamine coated stabilized PAN NFs were dried overnight in an oven at 80 °C and then impregnated in aqueous solutions of 0.5 M FeCl$_3$ and 1 M NiCl$_2$. After 12 h, the NFs were collected by rotatory evaporator and dried overnight at 80 °C in an oven. Finally, these were heat treated in a tube furnace at 800 °C for 2 h under Ar atmosphere with an initial ramp of 4 °C min^{-1}. Two different sample morphologies were obtained depending on the melamine to metal salts molar ratio; (i) needle-like FeNi embedded in graphene sheets which were wrapped over N-doped CNFs (labelled as GS@NCNF) at 3 : 2 ratio and (ii) bamboo-shaped CNTs and GNTs over N-doped CNF with spherical FeNi NPs encapsulated at CNT tips (labelled as G/CNT@NCNF) at 3 : 1 ratio, respectively. Both samples showed trace amount of oxide formation. Samples were also treated with 69 wt% HNO$_3$ at 80 °C for 8 h under reflux conditions and washed several times with deionized water until pH of the filtrate became neutral. The corresponding acid treated samples were labelled as AT-GS@NCNF and AT-G/CNT@NCNF.

2.2. Physical and chemical characterization

The surface morphology of the samples was examined by field emission scanning electron microscopy (FE-SEM) using FEI NOVA NanoSEM 450. The internal structure was studied by transmission electron microscopy (TEM) using JEOL JEM 2010. The phases were identified by X-ray diffraction (XRD) using Philips PAN analytical powder system. The surface chemical states were investigated by X-ray photoelectron spectroscopy (XPS) using Scienta 300 spectrometer. The specific surface area and pore sizes were determined using Brunauer–Emmett–Teller (BET) method from nitrogen adsorption–desorption data recorded with Micromeritics ASAP 2020.

2.3. Electrochemical characterization for ORR and OER

The electrochemical measurements were performed on a bipo-tentiostat (WaveDriver 20) with a three electrode cell at room temperature. A glassy carbon electrode (GCE), rotating disk electrode (RDE) and rotating ring disk electrode (RRDE) loaded with the catalyst was used as the working electrode. A saturated calomel electrode (SCE) and Pt wire served as the reference and counter electrodes, respectively. All the potentials were initially measured against SCE and then converted to reversible hydrogen electrode (RHE) using the relation: $E_{RHE} = E_{SCE} + 0.241 + 0.059\text{pH}$. For preparing the catalyst ink, 5 mg of the sample was gently grinded into fine powder and dispersed in 500 μl mixture of ethanol and DI water (1 : 1) and 30 μl Nafion solution by 30 min ultrasonication. Then, 10 μl of the catalyst slurry was dropped on the working electrode and dried in air (mass loading: 0.400 mg cm^{-2}). The electrolyte was saturated by bubbling O_2 (or N_2) for at least 20 min. Before recording the cyclic voltammogram (CV) data, the working electrode was cycled 50 times at a scan rate of 50 mV s^{-1} under N_2 purging. CVs of all the samples were obtained in O_2 saturated 0.1 M KOH at a scan rate of 10 mV s^{-1}. Linear sweep voltammetry (LSV) was performed on RDE at 400, 800, 1200, 1600, 2000 and 2400 rpm. Durability tests of G/CNT@NCNF, AT-G/CNT@NCNF and Pt/C were performed using the current–time chronoamperometric technique at 0.7 V (*vs.* RHE). Methanol crossover tolerance of all samples was evaluated in the presence of 3 M methanol with continuous bubbling of O_2 into the electrolyte. OER measurements were performed using GCE, Hg/HgO and Pt wire as the working, reference and counter electrode, respectively, in 1 M KOH. Electrode ink was prepared by dispersing 5 mg of the catalyst in 1 mL of ethanol and isopropanol (1 : 1) mixture with 30 μl of 0.5 wt% Nafion as binder. The mixture was sonicated for 3 h at room temperature to prepare a homogenous dispersion. 10 μl of the prepared electrode ink was casted on the GCE (0.71 mg cm^{-2} loading). The electrochemical active surface area (ECSA) of G/CNT@NCNF and GS@NCNF samples were calculated by using the relation: ECSA = C_{DL}/C_s where C_{DL} is the double layer capacitance and C_s is the specific capacitance. For FeNi the reported value of C_s is around 40 μF in alkaline conditions.[37] Please see ESI† for these calculations.

3. Results and discussion

3.1. Morphology and structure

Electrochemical characteristics of carbon nanostructures depend on the synthesis method which controls the morphology and type of nitrogen doping in the carbon lattices. Transition metal/alloy sources have been used as catalyst for carbon nanostructure growth, which can be beneficial to the electrochemical catalytic activity for ORR/OER.[38,39] In this study, the melamine-coated stabilized PAN NFs are transformed to N-doped CNFs by carbonization heat treatment and FeNi NPs acts as the catalyst for carbon nanostructure growth on the CNF surfaces. Fig. 2 shows the SEM and TEM images to observe the surface morphology and internal structure of GS@NCNF and G/CNT@NCNF, respectively. It is clearly found that two distinct

structures were formed depending on the molar ratio of melamine to metal salts. The ratio of 3 : 2 exhibits needle-like FeNi (mean aspect ratio ≈ 10 ± 3 (Fig. S1†)) covered with ∼5 nm thick graphene sheets which were wrapped over CNFs. To form graphitic carbon sheets, melamine decomposes into gaseous species such as $C_2N_2^+$, $C_2N_3^+$, and $C_3N_3^+$, which diffuses into the metal alloy NPs to form complexes like metal carbides.[34,40] The metal carbides catalyze the formation of graphitic carbon. The HR-TEM image in Fig. 2c shows the FeNi needle like structure adjacent to the ∼5 nm thick graphene where lattice spacing of 0.208 and 0.34 nm is observed for (111) plane of fcc-FeNi and (002) plane of graphene, respectively. In addition, a lattice spacing of 0.24 nm for (222) plane of $NiFe_2O_4$ was observed but near the edges of the FeNi needle. This was further investigated by FFT of the HR-TEM image taken near the GS and needle-like structures, where (111) and (220) plane of $NiFe_2O_4$ along with (002) plane of graphene were observed (Fig. 2d). The observation of trace amount of oxides will be discussed later in the XPS results.

By changing the molar ratio of melamine to metal salts to 3 : 1, the growth of CNTs and GNTs were observed with spherical metal alloy NPs enclosed in the ∼10 nm thick graphene layers at the CNT tips as shown in the SEM and TEM image in Fig. 2e and f, respectively. Here, the average diameter of CNTs is 105 ± 22 nm (Fig. S1†) with lengths of several μm and majority of the alloy NPs were encapsulated at the CNT tips (Fig. 2g). Majority of the CNTs are bamboo-shaped (Fig. 2h), which is a characteristic of the N-doped CNTs with number of cages connected continuously with each other. Liu *et al.* investigated the role of melamine concentration on the structure and morphology of N-doped CNTs synthesized by CVD.[41] The report described that the outer diameter of CNTs increases and the structure changes from straight morphology to more rough and bamboo-like morphology with increasing melamine concentration. Different bond lengths of the C–N and C–C bond also favor the formation of bamboo-shaped morphology.[41,42] In addition, the formation of GNTs was observed in Fig. 2f, which is similar to the observations by Gupta *et al.*[34] and Fan *et al.*[40] GNT can be defined as a structure with larger diameter (∼300 nm) and thinner walls compared to CNTs, and is beneficial for the electrocatalytic activity by improving the mass transport and ion exchangeability between the surface and inner layers of GNTs.[43] The SEM image and elemental map of G/CNT@NCNF in Fig. 2i confirms the well-mixed state of Fe and Ni in the NPs with stronger C signal coming from the super-saturation and graphene encapsulation of NPs.

The crystalline nature of the FeNi alloy and carbon nanostructures were investigated by X-ray powder diffraction as shown in Fig. 3a. Both G/CNT@NCNF and GS@NCNF showed peaks at 43.38°, 50.67°, and 74.49° corresponding to (111), (200) and (220) planes of fcc FeNi alloy (JCPDS – 47-1417), respectively. In addition, peaks at 26.48°, 44.60° and 54.54° represent (002), (101) and (004) planes of the graphite and turbostratic carbon (JCPDS-041-1487), respectively. After acid treatment, the FeNi metal alloy peaks disappear almost completely. No secondary peaks were detected in XRD although TEM and XPS analysis (discussed later) confirmed trace amount of $NiFe_2O_4$
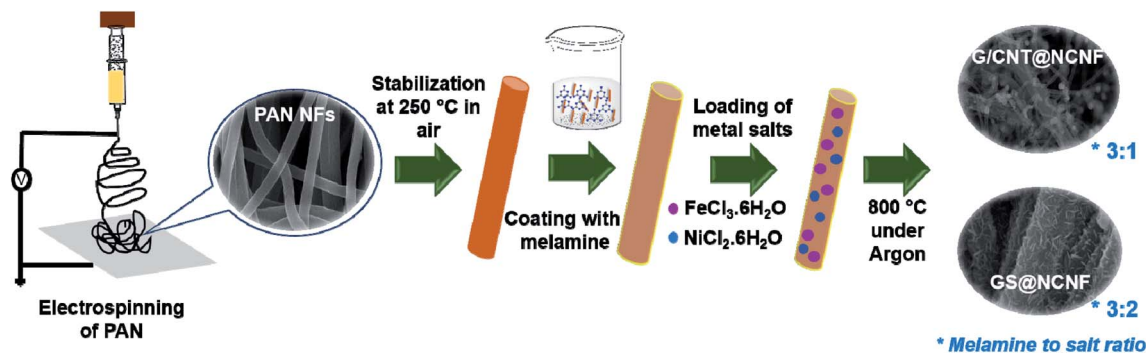
Fig. 1 Schematic of the synthesis process involving electrospinning of PAN solution, coating with melamine and metal salts and heat treatment to produce two distinct morphologies depending on the melamine to salt ratio.

with spinel structure existed in the samples. Fig. 3b shows Raman spectra of the samples to investigate the extent of graphitization and defects in the hybrid nanostructures with the two characteristic peaks; D-band at ~1350 cm^{-1} and G-band at ~1560 cm^{-1}. The G-band is assigned to the graphitic E$_{2g}$ mode for the in-plane bond-stretching of a pair of sp^2 carbon atoms, while the D-band is attributed to the breaking of the symmetry caused by structural disorder and defects.[44] A relatively higher peak intensity ratio I_D/I_G, indicative of the higher number of defective sites in the carbon structure,[45] was observed for all the samples which is beneficial for the electron transfer kinetics.[46] The I_D/I_G ratio for G/CNT@NCNF decreased from 1.4 to 1.07 after acid treatment due to removal of amorphous and defective carbon from the CNF surfaces, thus, increasing the relative graphitic content.[47] In contrast, acid treatment increased the I_D/I_G ratio from 1.11 to 1.21 for GS@NCNF, which may be due to the removal of FeNi embedded graphene sheets from the CNF surfaces (Fig. S2†). Hierarchically porous structure with high specific surface area are desired for more active sites and efficient reactant/product transport.[48]
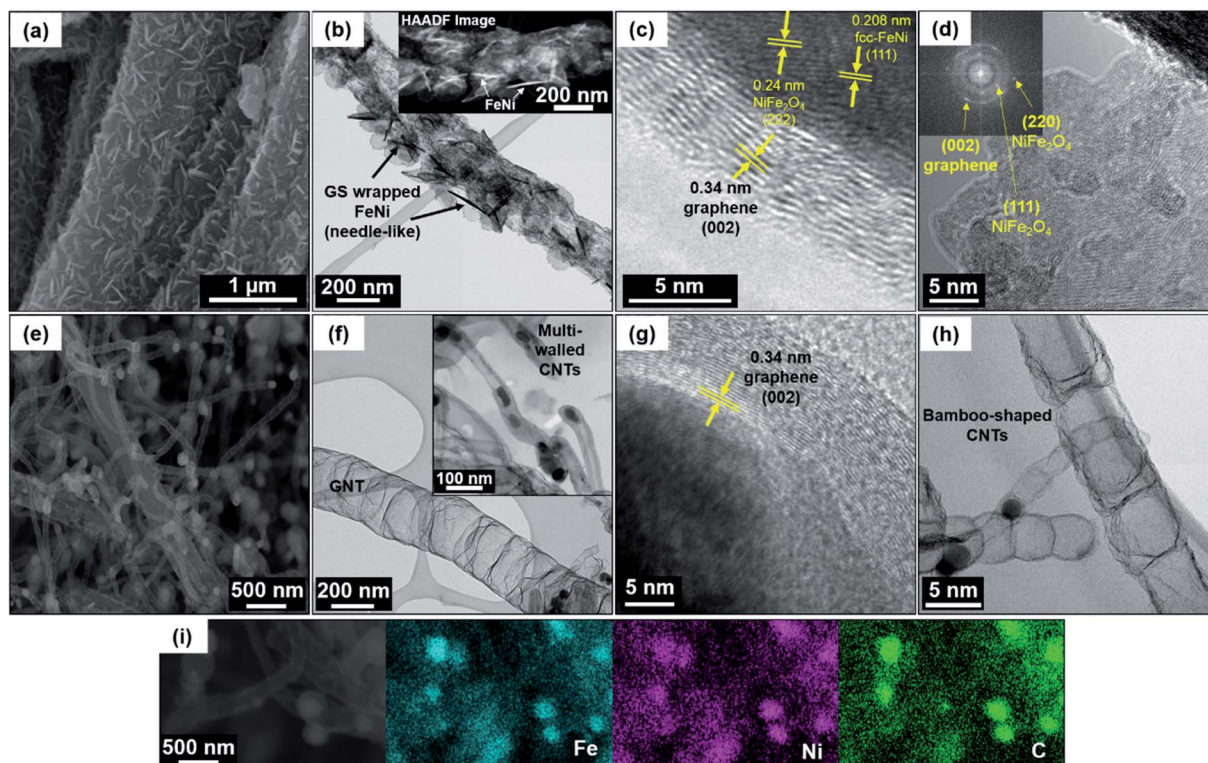

Fig. 2 (a) SEM and (b) TEM images of GS@NCNF sample showing the needle-like FeNi over CNF surfaces (inset: HAADF image) and corresponding (c and d) HR-TEM images near the interface of FeNi and graphitic sheets. (e) SEM and (f) TEM images of G/CNT@NCNF sample showing a mixture of GNTs and CNTs (inset) on the CNF surfaces and corresponding (g) HR-TEM image of a CNT tip showing ~10 nm thick graphene layer. (h) Characteristic bamboo-shaped morphology of CNTs seen in TEM. (i) SEM image and the corresponding Fe, Ni & C EDX elemental maps for G/CNT@NCNF.
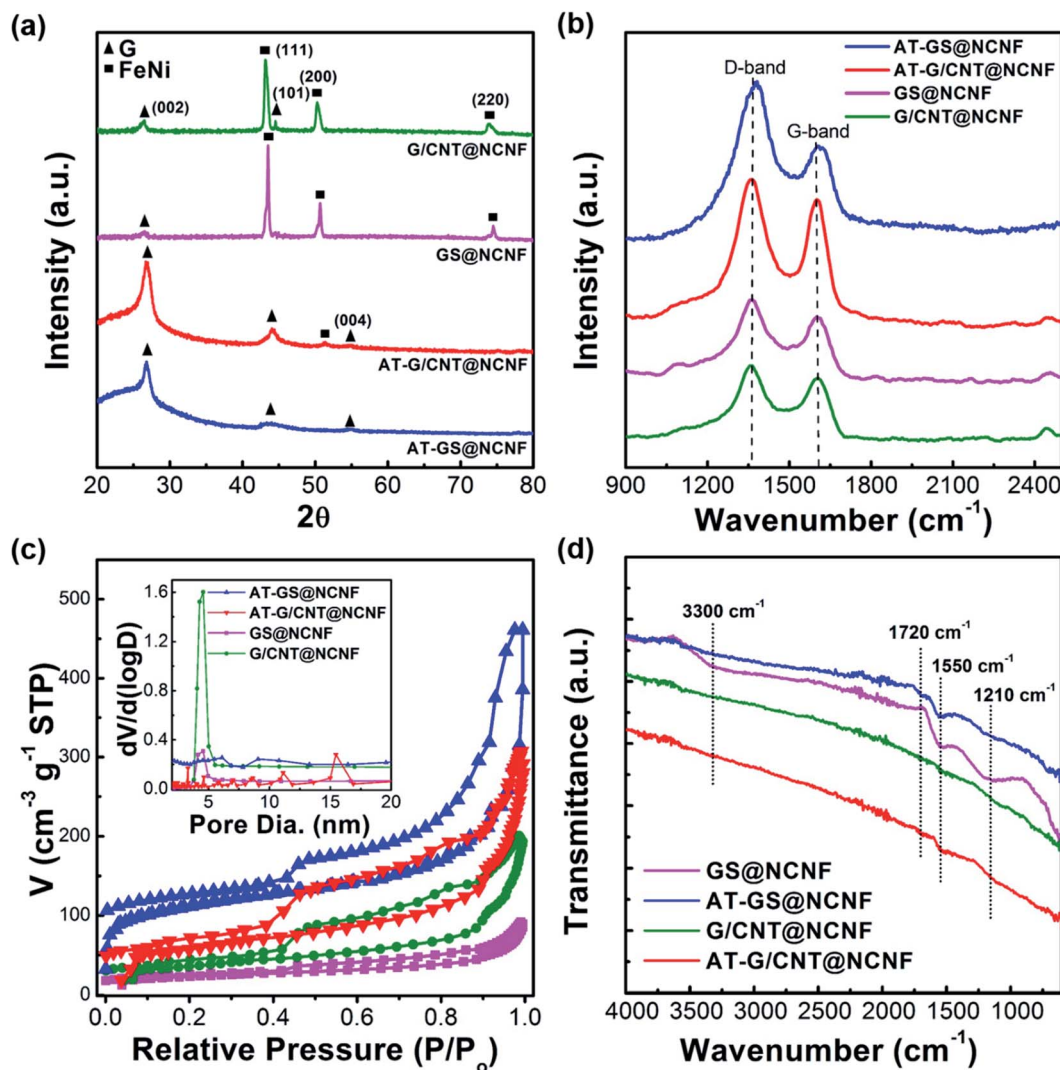
Fig. 3 (a) XRD scans, (b) Raman spectra, (c) Nitrogen adsorption–desorption isotherms at 77 K (inset shows the pore size distribution), and (d) IR spectra of the as-synthesized and acid treated catalysts.

Nitrogen adsorption–desorption measurements were performed at 77 K to investigate the S_{BET} and pore structure as shown in the Fig. 3c (inset shows the pore size distribution). All samples showed the typical hysteresis loop of type H4 between medium and high pressure range, which is attributed to the mesoporous structure with slit-like pores.[49] S_{BET} and average pore size was 80.3 m^2 g^{-1} and 15.0 nm for GS@NCNF, which was not changed significantly after acid treatment (83.7 m^2 g^{-1} and 15.0 nm). However, the S_{BET} was significantly increased from 133.7 m^2 g^{-1} to 213.85 m^2 g^{-1} for the G/CNT@NCNF where most of FeNi NPs leached from the CNTs, accompanied with a negligible decrease in the average pore size from 11.3 nm to 10.5 nm.

3.2. Surface chemical states

IR analysis in Fig. 3d was performed to identify the type of functionalities on the surfaces. GS@NCNF exhibited three clear broad peaks around 3300 cm^{-1} (OH), 1550 cm^{-1} (C=C and C=

N) and 1210 cm^{-1} (C–O–C), whilst the rest of the samples showed much less intensities or complete absence of these three peaks. The acid-treated samples (AT-GS@NCNF & AT-G/CNT@NCNF) showed very weak peaks around 1550 cm^{-1} and 1720 cm^{-1} due to C=C and C=O formation, respectively. Thus, GS@NCNF has significant amount of oxygen functionalities as part of the graphitic carbon structure,[50] which is further supported by the XPS analysis discussed next.

XPS was performed to evaluate compositions of the samples and chemical states of each element. Fig. 4a shows the survey scans with three distinct peaks of C, N, O in all the samples and additional Fe and Ni peaks in G/CNT@NCNF and GS@NCNF. The atomic percentages are listed in the Table 1. The Fe 2p spectrum in Fig. 4b splits into two peaks centered at 711 eV and 724.8 eV due to the spin orbital coupling. The deconvolution revealed presence of Fe^0 for G/CNT@NCNF sample with peak at 705.82 eV. Both G/CNT@NCNF and GS@NCNF showed Fe^{3+} (711.11 eV and 724.11 eV), Fe^{3+} satellite peak (720 eV), and Fe^{2+}
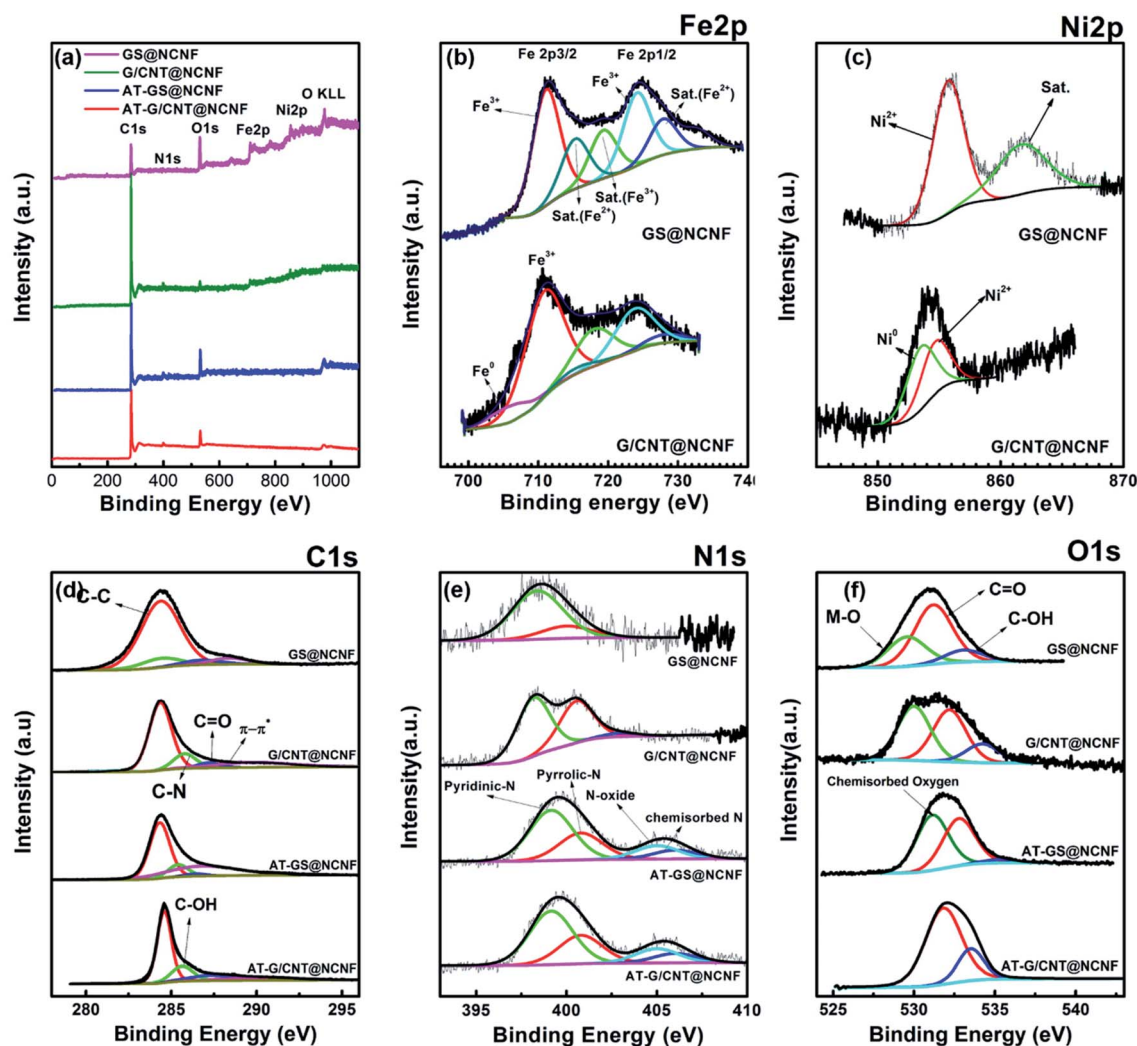
Fig. 4 (a) XPS survey scan and high resolution spectra of (b) Fe 2p, (c) Ni 2p, (d) C 1s, (e) N 1s, and (f) O 1s.

Table 1 The atomic percentages (at%) of the samples determined from the XPS analysis

Sample IDs	C	O	N	Fe	Ni
G/CNT@NCNF	92.41	3.59	2.62	1.22	0.17
GS@NCNF	64.63	24.24	1.54	8.27	1.32
AT-G/CNT@NCNF	87.36	8.97	3.67	—	—
AT-GS@NCNF	82.53	11.75	5.72	—	—

satellite peaks (715.27 eV and 727.87 eV),[51,52] which can be ascribed to the presence of oxide, most probably $NiFe_2O_4$ as observed in the HR-TEM. Ni 2p high resolution spectra in Fig. 4c showed Ni^{2+} at 855.74 eV with a satellite peak at 862 eV for GS@NCNF. However, the G/CNT@NCNF showed the presence of both Ni^0 and Ni^{2+} at 853.2 eV and 854.91 eV, respectively.[53] These results support the formation of FeNi bimetallic alloy along with trace amount of $NiFe_2O_4$ (more pronounced in GS@NCNF) due to the detection of surface Ni^{2+} and Fe^{3+} states. The reason why the peaks associated with such oxides were not found in the XRD patterns is due to their trace amounts.

The deconvoluted high resolution spectra of C 1s in Fig. 4d reveals the presence of four prominent species; C=C/C–C, C–N, C=O, C–OH for both metal-containing samples. The presence of C=O and C–OH improves hydrophilicity, enhances the transport of reactants, and increases the catalytically active sites.[54] The peak at 286.4 eV is due to C–N which also confirms the N doping in the hybrid catalysts.[55,56] Nitrogen doping in carbon plays an important role in improving the oxygen electrolysis performance by controlling the electronic conductivity, the number of active sites, and even the oxidation resistance of carbon.[57] Nitrogen, especially pyridinic-N, coordinates with the metal by forming M–N bond which reduces the contact resistance and improves the mass transport.

The N 1s high resolution spectra (Fig. 4e) of G/CNT@NCNF and GS@NCNF showed peaks at 398.3 eV and 400.6 eV representing the presence of pyridinic-N and pyrrolic-N, respectively.[58,59] After acid treatment, the N-oxide and chemisorbed-N species were also detected at 404.9 eV and 406.1 eV, respectively.[60] The O 1s spectra in Fig. 4f revealed the presence of C=O and –OH functionalities for GS@NCNF (531.27 eV and 533 eV)
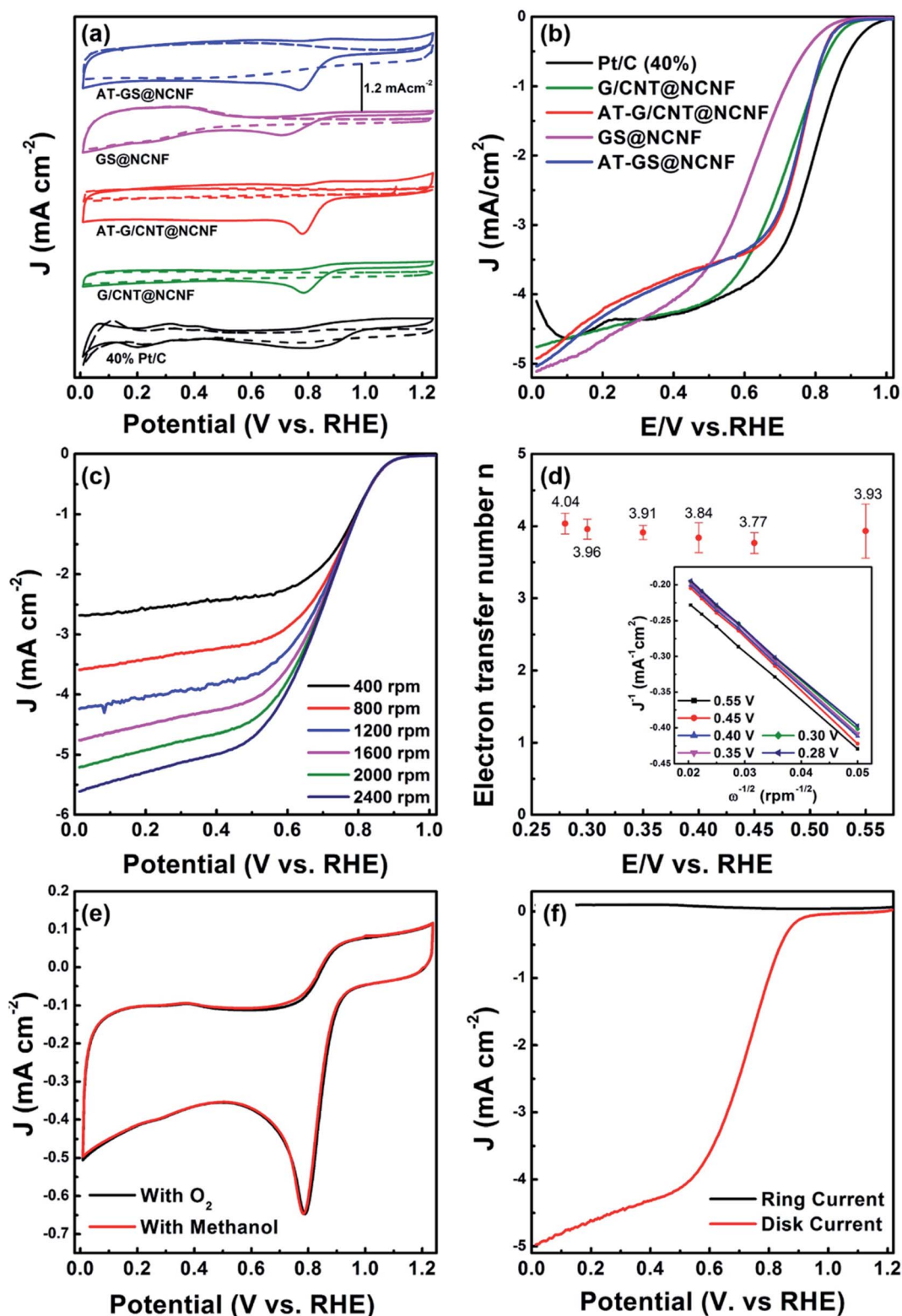
Fig. 5 (a) CV and (b) LSV at 1600 rpm for all the samples. (c) LSV at various rotating speeds for G/CNT@NCNF. (d) Electron transfer number 'n' and corresponding K−L plots (inset) of the G/CNT@NCNF. (e) CV of G/CNT@NCNF in O_2-saturated 0.1 M KOH and methanol at a scan rate of 10 mV s^{-1}. (f) RRDE voltammograms in O_2-saturated 0.1 M KOH at 1600 rpm and 10 mV s^{-1} with ring potential 0.5 V.

and G/CNT@NCNF (532.2 eV and 534.2 eV), respectively. Furthermore, the peaks around 529.5 eV for both GS@NCNF and G/CNT@NCNF indicate the presence of oxygen associated with the metal species as indicated by HR-TEM in Fig. 1c and d for GS@NCNF. After acid treatment the peak for metal oxide completely disappeared due to the complete (GS@NCNF) or
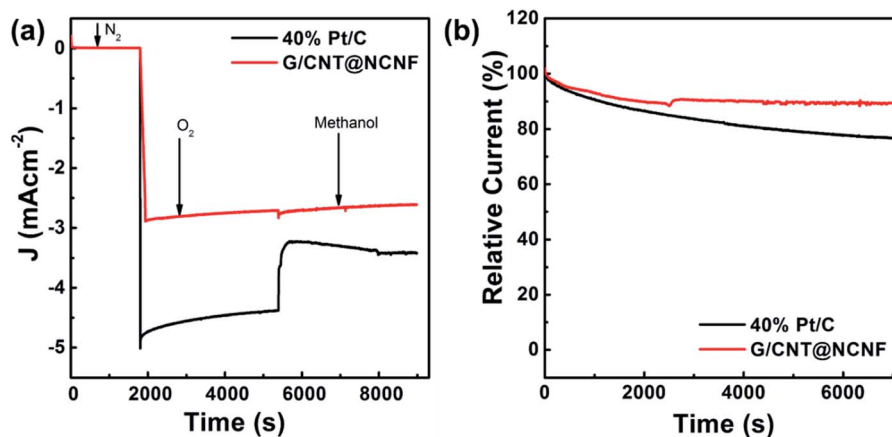
Fig. 6 (a) Current–time chronoamperometric response of G/CNT@NCNF and 40% Pt/C at 1600 rpm. The arrows indicate the introduction of N_2, O_2 and methanol. (b) Current–time chronoamperometric response of G/CNT@NCNF and 40% Pt/C at 1600 rpm in O_2-saturated 0.1 M KOH at a potential of 0.7 V $vs.$ SCE.

Fig. 7 (a) LSV polarization curves for the synthesized and acid treated samples in 1 M KOH and (b) corresponding Tafel slopes. (c) EIS of GS@NCNF, G/CNT@NCNF and AT-G/CNT@NCNF. (d) Chronopotentiometry response ($E-t$) of G/CNT@NCNF and GS@NCNF at 10 mA cm^{-2}.

Fig. 8 CV in 0.92–1.08 V *versus* RHE for (a) G/CNT@NCNF and (b) GS@NCNF in 1 M KOH. (c) Dependence of current density on the scan rate at 1.003 V *versus* RHE.

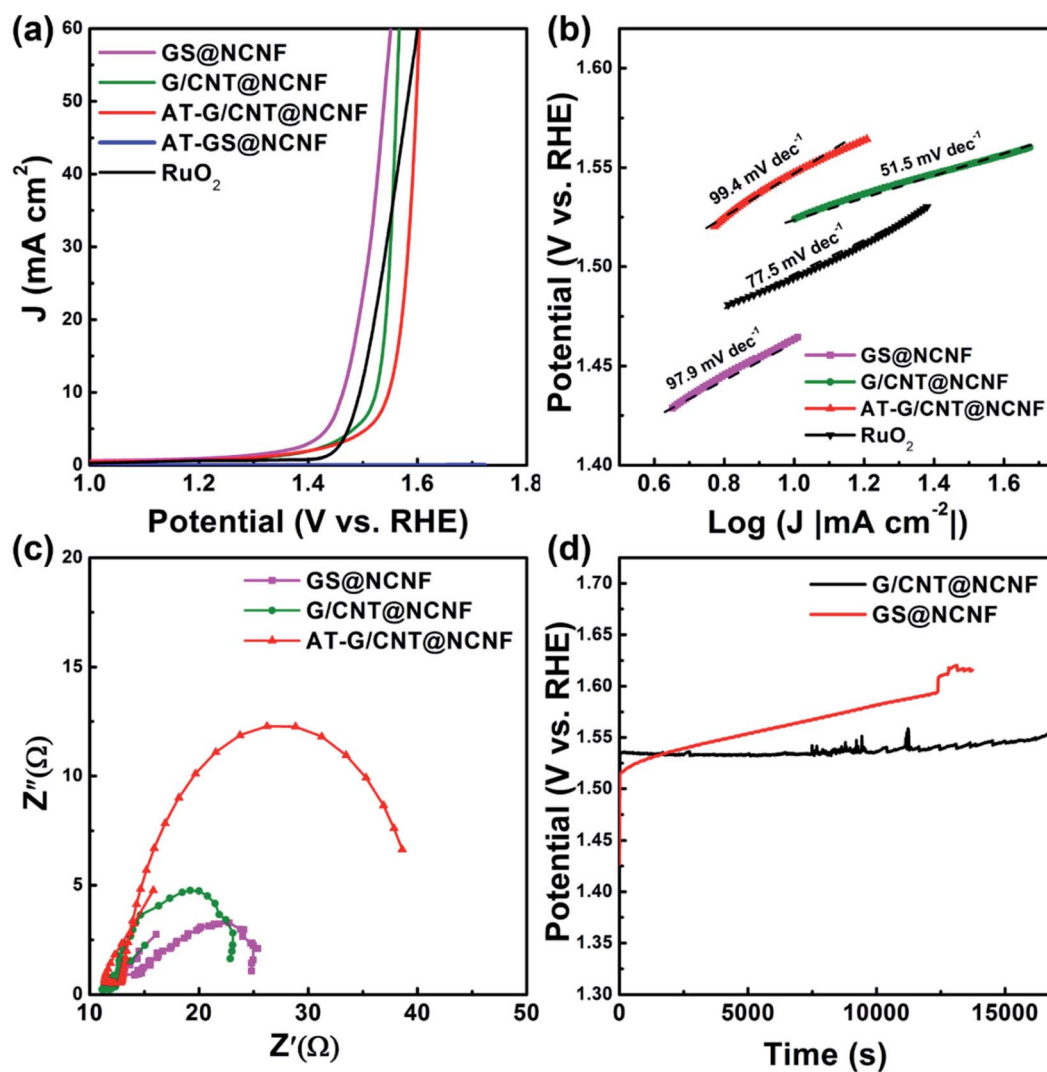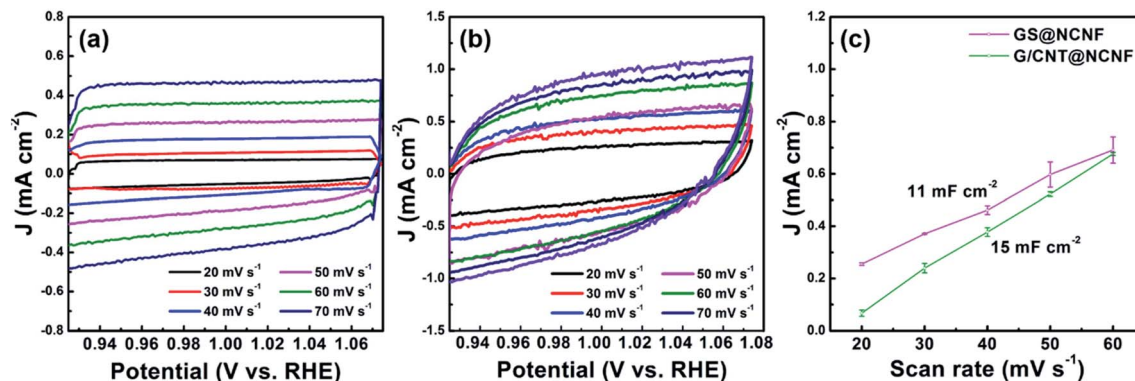partial (G/CNT@NCNF) removal. The oxygen concentration in AT-GS@NCNF also decreased from 24% to 11%. However, the oxygen concentration increased for AT-G/CNT@NCNF from 3.59% to 8.97% which is due to the functionalization of NTs,[61] which is beneficial for electrocatalysis.[62] Also, the concentration of hydrated metal salts is high in the GS@NCNF which could result in higher oxygen groups containing functionalities on GS (as observed in the IR analysis) and partial oxidation of FeNi NPs as seen in the TEM and XPS analysis. XPS generally probes 1–10 nm depth whereas our synthesized samples are hierarchical in nature with length scales up to few hundred nm which makes XPS data analysis and interpretation challenging in the present study.

3.3. ORR activity

CV and LSV measurements were performed in O_2 and N_2 saturated 0.1 M KOH solution at a scan rate of 10 mV s^{-1}. Fig. 5a shows the CV plots for all the catalysts with oxygen reduction peak in 0.71–0.79 V range *vs.* RHE in O_2 saturated electrolyte, whereas no peaks were observed in the N_2 saturated environment (dashed data). The onset potential (E_{onset}), half-wave potentials ($E_{1/2}$), and current densities ($J_{0.4V}$) acquired from the LSV measurements is summarized in Table S1† and Fig. 5b shows the LSV data at 1600 rpm only. Among all the catalysts, G/CNT@NCNF showed superior activity with E_{onset} and $E_{1/2}$ of 0.948 V and 0.74 V *vs.* RHE and a limiting current density similar to Pt/C. The 40% Pt/C exhibits ORR peak around 0.85 V *vs.* RHE under similar testing conditions with E_{onset} and $E_{1/2}$ of 1.01 V and 0.79 V, respectively. Such high ORR activity of G/CNT@NCNF can be ascribed to the synergistic effect of N-doped CNTs along with GNTs and FeNi metal alloy NPs encapsulated in the graphene layers at CNT tips. The large diameter of GNTs (~300 nm) provides high surface area, which promotes mass transfer and offer more active sites for catalysis.

LSVs from 400–2400 rpm are shown in the Fig. S3–S5† for the remaining samples. Current densities increased with rotation speed due to shortening of the diffusion distances.[63] After acid treatment, the E_{onset} of G/CNT@NCNF decreased from 0.948 V to 0.928 V along with the limiting current density (Fig. S4†). The GS@NCNF sample after acid treatment underwent removal of

needle-like FeNi along with graphene sheets as seen in the SEM image in Fig. S2.† The improvement in activity (Fig. S5†) of the AT-GS@NCNF can be attributed to higher N-doping and introduction of defects as confirmed by I_D/I_G value of 1.2 from the Raman analysis.[64] Acid treatment imparts additional N functionalities on the surfaces as evident from the XPS analysis. The increased N-doping, despite removal of FeNi embedded GS, originates from PAN which is used as the precursor for CNFs. Previous studies indicate that N-doping plays a significant role in ORR by reducing the C–N bond length as compared to the O–O bond.[65,66] which facilitates the adsorption, desorption and reduction of dioxygen into water.[67] The electrocatalytic activity for both acid treated catalysts is similar where higher N-doping and defects in AT-GS@NCNF and more than twice specific surface area in AT-G/CNT@NCNF are the dominating factors.

To study the ORR electron transfer pathway for G/CNT@NCNF, the Koutecky–Levich plots (j^{-1} *vs.* $\omega^{-1/2}$) were obtained from the LSVs corresponding to currents at 0.65, 0.55, 0.45, 0.40, 0.35 and 0.30 V (*vs.* RHE) as shown in the Fig. 5d (inset). The electron transfer number 'n' of ORR is obtained from the slope of K–L plots which varied from 3.75–4.0. For all catalysts K–L plots are linear in potential range of 0.3–0.55 V which signifies that 4e$^-$ pathway is predominant (Fig. 5d, S3c, S4c and S5c†). To verify the amount of H_2O_2 generated during ORR a rotating ring-disk electrode (RRDE) was employed. Fig. 5f shows that for G/CNT@NCNF, there is significantly high limiting current density from the disk for ORR with extremely low current density corresponding to H_2O_2 oxidation on the Pt-ring electrode at 1600 rpm. Moreover, significant decrease in H_2O_2 production is observed for samples without acid treatment (Fig. S6†). The present results are consistent with previous findings where H_2O_2 production is decreased from 20% to 6% upon incorporation of metal in N-doped carbon materials.[68]

Hydrocarbon fuels such as methanol or ethanol can be used in fuel cell systems instead of hydrogen, which gives added advantage in terms of fuel flexibility. When methanol is used as a fuel, it could cross over through the electrolytes from anode to cathode. This degrades the overall cell performance in short-time operation due to poisoning or degradation of the cathodes. That is why the catalytic selectivity of the cathode is

important for stable methanol-based fuel cells.[63] To confirm stability of the prepared catalysts for methanol, CVs were measured with and without addition of methanol (Fig. 5e, S4f, and S5f†). It was further assessed by chronoamperometry in Fig. 6a which shows stable activity of G/CNT@NCNF for ORR with high current density even after adding methanol, whereas Pt/C was unstable due to methanol oxidation. High durability of G/CNT@NCNF was also tested in O_2 saturated 0.1 M KOH at a potential of 0.7 V vs. SCE which showed only 10% degradation in current density compared to 26% degradation for Pt/C (Fig. 6b). These results indicate much better methanol tolerance and durability of the synthesized hybrid catalysts compared to Pt/C.

3.4. OER activity

Electrolysis is a promising technology for hydrogen production from water, but OER has been considered as a rate-determining step due to sluggish kinetics than hydrogen evolution. Fig. 7a shows OER activity of all samples in 1 M KOH solution. GS@NCNF exhibits the highest activity with low over-potential (η) of ~230 mV at 10 mA cm^{-2} whereas G/CNT@NCNF and AT-G/CNT@NCNF exhibited slightly higher η of ~290 mV and ~320 mV at 10 mA cm^{-2}, respectively. Significantly low OER activity of AT-GS@NCNF may be due to leaching out of FeNi with acid treatment as mentioned above. However, G/CNT@NCNF still showed OER activity after acid treatment, which may be attributed to residual FeNi NPs encapsulated by graphitic layers.[69] Pumera et al.[70] reported 88% removal of metal by the similar acid treatment used in this study. Generally, FeNi and FeCo are regarded as excellent OER catalysts but sole use of them without an efficient support rendered poor long-term performance because of poor electronic conduction and metal-support interaction. The FeNi NPs embedded on NCNF could result in the improved catalytic activity.[71] Besides, the N-doped carbons typically show comparable ORR activity in alkaline solution without metal catalysts, whilst the OER activity is relatively dependent on the active sites of metal catalysts rather than those of N-doped carbons. The lower OER activity of the G/CNT@NCNF could be thicker graphene layers (~10 nm) that results in mass transport resistance compared to relatively thinner layers of GS@NCNF (~5 nm). The activity of the prepared catalysts for OER is compared with similar materials reported in literature (Table S3†) where our GS@NCNF and G/CNT@NCNF showed excellent activity with a low over-potential of 230 mV and 290 mV with corresponding Tafel slopes of 97.9 mV dec^{-1} and 51.5 mV dec^{-1}, respectively (Fig. 7b). The Tafel slope gives insight about the electrochemical reaction kinetics. Although there are numerous explanations for the Tafel slope values, kinetics for O–O bond formation process, which has been considered as a rate-determining step for OER in alkaline solution such as $O + O \rightarrow O_2$ or $H_2O + O \rightarrow OOH + H^+ + e$, can be estimated using it. The lower value of G/CNT@NCNF than 77.9 mV dec^{-1} of RuO_2 can therefore indicate improved kinetics of the former than the latter. The lower Tafel slope of G/CNT@NCNF can be attributed to the presence of CNTs and GNTs on CNFs which not only increases the surface

area but also improves the conductance due to high graphitic contents.

Electrochemical impedance spectroscopy (EIS) was performed to evaluate the conductive nature of the electrocatalysts. Nyquist plots are obtained at 0.65 V versus Hg/HgO reference electrode to calculate the interfacial charge transfer resistance (R_{ct}) as shown in the Fig. 7c. The smaller the characteristic semicircle formed in the Nyquist plots faster the kinetics. GS@NCNF and G/CNT@NCNF show R_{ct} value of 12.34 Ω and 11.75 Ω, respectively, whereas it increases for AT-G/CNT@NCNF to 27.27 Ω. To evaluate the durability of the catalysts, chronopotentiometry was performed for G/CNT@NCNF and GS@NCNF at current density of 10 mA cm^{-2} on GCE for 4 h. Fig. 7d revealed that G/CNT@NCNF retained the potential for longer period of time as compared to GS@NCNF which shows continuous increase in the overpotential for OER despite an initial low overpotential. This can be attributed to the harsh effects produced by strong alkaline media which structurally degrades the hybrid structure as seen in the SEM image in Fig. S7.† Metal dissolution in strong alkaline solution could be prevented by the graphene layers covering metal NPs. As shown in the TEM images, 10 nm thick graphene layers of G/CNT@NCNF can more effectively protect NPs from dissolution in alkaline solution compared to 5 nm thick layers of GS/NCNF, which may be why the former showed lower OER activity in initial stage, but higher stability during operation.

Electrochemical active surface area (ECSA) and double layer capacitance of the catalysts can be calculated by taking CV scans between 0.92–1.08 V potential vs. RHE as shown in Fig. 8(a and b). Fig. 8c represents the plot between the current densities at 1.003 V (vs. RHE) and the scan rate in 20–60 mV s^{-1} range with the slope corresponding to the double layer capacitance. Here, again G/CNT@NCNF outperforms GS@NCNF with high double layer capacitance i.e. 15 mF cm^{-2} vs. 11 mF cm^{-2}, respectively. The ECSA, using the C_{DL} values, for G/CNT@NCNF and GS@NCNF are 37.5 cm^2 and 27.5 cm^2, respectively. The structural differences between the two catalysts are important with CNTs & GNTs improving the ECSA. The catalytic activity of catalysts depend on several other factors as well e.g. coordination of metal with carbon, type of N-doping, conductivity of carbon materials and number of defect sites.[69,72]

The above electrochemical results show that morphology of nanostructures formed after carbonization process plays a significant role in determining the overall catalytic activity of catalysts and their durability for ORR and OER. Despite of the lower over potential of GS@NCNF in OER, it is not very stable over time and exhibits low conductivity as compared to catalysts containing nanotubes. The onset potential in OER depends on the vacant d-orbitals of metal alloy available for interaction with the reacting species. During the CNTs formation the C from the precursor diffuses on metal NPs surface and form metal–C bonds. The bimetallic NPs enclosed at CNT tips show moderately less activity but exhibit better long term stability. For GS@NCNF, the mixture of FeNi with oxide, most probably $NiFe_2O_4$, boosts the intrinsic activity of FeNi and helps to stabilize the active sites.[73] Table S1† lists overvoltage (ΔE) between E_{OER} and E_{ORR} for all the catalysts to assess the

efficiency loss during the bifunctional OER/ORR activity. The smaller the overpotential lesser the loss in efficiency. G/CNT@NCNF shows the smallest ΔE of 0.78 V which is attributed to the effective mass and electron transfer, N-doping, enhanced surface area and availability of the active sites by CNTs and GNTs.

4. Conclusion

In summary, we have designed two different morphologies of bimetallic FeNi loaded carbon nanostructures as bifunctional catalyst for OER and ORR *via in situ* growth during high temperature carbonization of the stabilized PAN NFs coated with melamine and metal salts. The G/CNT@NCNF exhibited good electrocatalytic activity for ORR with an E_{onset} difference of only 62 mV compared to Pt/C, superior stability and methanol tolerance. The superior ORR performance is mainly attributed to the effect of N-doped CNFs, unique mixture of CNTs and GNTs, and FeNi NPs which provide more favorable active sites and facilitates both the electron and mass transfer. Similarly, for OER GS@NCNF show low overpotential of 230 mV at 10 mA cm^{-2} but is not very stable over time. G/CNT@NCNF has slightly more over-potential (60 mV) but is very stable with low Tafel slope of 51.5 mV dec^{-1} and high ECSA. The differences in the graphene layer thickness in the two samples also affect OER and ORR activities. The facile synthesis process reported here needs to be further explored to design unique hierarchical carbon based materials containing metal species for enhanced electrocatalytic performance.

Conflicts of interest

There are no conflicts of interest to declare.

Acknowledgements

References

1 S. Chu and A. Majumdar, Opportunities and Challenges for a Sustainable Energy Future, *Nature*, 2012, **488**(7411), 294–303, DOI: 10.1038/nature11475.

2 O. Ellabban, H. Abu-Rub and F. Blaabjerg, Renewable Energy Resources: Current Status, Future Prospects and Their Enabling Technology, *Renewable Sustainable Energy Rev.*, 2014, **39**, 748–764, DOI: 10.1016/j.rser.2014.07.113.

3 Y. Jiao, Y. Zheng, M. Jaroniec and S. Z. Qiao, Design of Electrocatalysts for Oxygen- and Hydrogen-Involving Energy Conversion Reactions, *Chem. Soc. Rev.*, 2015, **44**(8), 2060–2086, DOI: 10.1039/c4cs00470a.

4 M. Sharma, N. Jung and S. J. Yoo, Toward High-Performance Pt-Based Nanocatalysts for Oxygen Reduction Reaction through Organic-Inorganic Hybrid Concepts, *Chem. Mater.*, 2018, **30**(1), 2–24, DOI: 10.1021/acs.chemmater.7b03422.

5 M. K. Kayarkatte, Ö. Delikaya and C. Roth, Freestanding Catalyst Layers: A Novel Electrode Fabrication Technique for PEM Fuel Cells via Electrospinning, *ChemElectroChem*, 2017, **4**(2), 404–411, DOI: 10.1002/celc.201600530.

6 G. Ercolano, F. Farina, S. Cavaliere, D. J. Jones and J. Rozière, Towards Ultrathin Pt Films on Nanofibres by Surface-Limited Electrodeposition for Electrocatalytic Applications, *J. Mater. Chem. A*, 2017, **5**(8), 3974–3980, DOI: 10.1039/C6TA09016H.

7 M. T. Sung, M. H. Chang and M. H. Ho, Investigation of Cathode Electrocatalysts Composed of Electrospun Pt Nanowires and Pt/C for Proton Exchange Membrane Fuel Cells, *J. Power Sources*, 2014, **249**, 320–326, DOI: 10.1016/j.jpowsour.2013.10.119.

8 A. Damjanovic, Y. I. Birss and D. S. Boudreaux, Electron Transfer Through Thin Anodic Oxide Films during the Oxygen Evolution Reactions at Pt Electrodes, *J. Electrochem. Soc.*, 1991, **138**(9), 2549.

9 T. Reier, M. Oezaslan and P. Strasser, Electrocatalytic Oxygen Evolution Reaction (OER) on Ru, Ir, and Pt Catalysts: A Comparative Study of Nanoparticles and Bulk Materials, *ACS Catal.*, 2012, **2**(8), 1765–1772.

10 N. Ma, Y. A. Jia, X. Yang, X. She, L. Zhang, Z. Peng, X. Yao and D. Yang, Seaweed Biomass Derived (Ni,Co)/CNTs Nanoaerogels: Efficient Bifunctional Electrocatalysts for Oxygen Evolution and Reduction Reactions, *J. Mater. Chem. A*, 2016, **4**(17), 6376–6384, DOI: 10.1039/C6TA00591H.

11 J.-C. Li, P.-X. Hou, S.-Y. Zhao, C. Liu, D.-M. Tang, M. Cheng and H.-M. Cheng, A 3D Bi-Functional Porous N-Doped Carbon Microtube Sponge Electrocatalyst for Oxygen Reduction and Oxygen Evolution Reactions, *Energy Environ. Sci.*, 2016, **9**(10), 3079–3084, DOI: 10.1039/C6EE02169G.

12 G. Ren, X. Lu, Y. Li, Y. Zhu, L. Dai and L. Jiang, Porous Core-Shell Fe$_3$C Embedded N-Doped Carbon Nanofibers as an Effective Electrocatalysts for Oxygen Reduction Reaction, *ACS Appl. Mater. Interfaces*, 2016, **8**(6), 4118–4125, DOI: 10.1021/acsami.5b11786.

13 J. Yang, T. Fujigaya and N. Nakashima, Decorating Unoxidized-Carbon Nanotubes with Homogeneous Ni-Co Spinel Nanocrystals Show Superior Performance for Oxygen Evolution/Reduction Reactions, *Sci. Rep.*, 2017, 7, 1–9, DOI: 10.1038/srep45384.

14 Y. Chen, Q. Liu and J. Wang, Highly Porous Nitrogen-Doped Carbon Nanofibers as Efficient Metal-Free Catalysts toward the Electrocatalytic Oxygen Reduction Reaction, *Nano Adv.*, 2016, **1**(2), 79–89, DOI: 10.22180/na174.

15 Y. Zhang, X. Zhuang, Y. Su, F. Zhang and X. Feng, Polyaniline Nanosheet Derived B/N Co-Doped Carbon Nanosheets as Efficient Metal-Free Catalysts for Oxygen Reduction Reaction, *J. Mater. Chem. A*, 2014, **2**(21), 7742–7746, DOI: 10.1039/c4ta00814f.

16 S. Yang, L. Zhi, K. Tang, X. Feng, J. Maier and K. Mellen, Efficient Synthesis of Heteroatom (N or S)-Doped Graphene Based on Ultrathin Graphene Oxide-Porous Silica Sheets for Oxygen Reduction Reactions, *Adv. Funct. Mater.*, 2012, **22**(17), 3634–3640, DOI: 10.1002/adfm.201200186.

17 K. Gong, F. Du, Z. Xia, M. Durstock and L. Dai, Nitrogen-Doped Carbon Nanotube Arrays with High Electrocatalytic Activity for Oxygen Reduction, *Science*, 2009, **323**(5915), 760–764.

18 X. Cui, S. Yang, X. Yan, J. Leng, S. Shuang and P. M. Ajayan, Pyridinic-Nitrogen-Dominated Graphene Aerogels with Fe–N–C Coordination for Highly Efficient Oxygen Reduction Reaction, *Adv. Funct. Mater.*, 2016, **26**(31), 5708–5717, DOI: 10.1002/adfm.201601492.

19 J. Li, S. Ghoshal, W. Liang, F. J. Moulay-Tahar Sougrati, B. Halevi, S. McKinney, G. McCool, C. Ma, X. Yuan, Z.-F. Ma, *et al.*, Structural and Mechanistic Basis for the High Activity of Iron-Nitrogen-Carbon Electrocatalysts toward Oxygen Reduction, *Energy Environ. Sci.*, 2016, **7**, 2418–2432, DOI: 10.1039/C6EE01160H.

20 M. Kobayashi, H. Niwa, M. Saito, Y. Harada and M. Oshima, Indirect Contribution of Transition Metal towards Oxygen Reduction Reaction Activity in Iron Phthalocyanine-Based Carbon Catalysts for Polymer Electrolyte Fuel Cells, *Electrochim. Acta*, 2012, **74**, 254–259, DOI: 10.1016/j.electacta.2012.04.075.

21 Q. Guo, D. Zhao, S. Liu, S. Chen, M. Hanif and H. Hou, Free-Standing Nitrogen-Doped Carbon Nanotubes at Electrospun Carbon Nanofibers Composite as an Efficient Electrocatalyst for Oxygen Reduction, *Electrochim. Acta*, 2014, **138**, 318–324, DOI: 10.1016/j.electacta.2014.06.120.

22 C. Ram, S. Sivamani, T. Micha Premkumar and V. Hariram, Computational Study of Leading Edge Jet Impingement Cooling with a Conical Converging Hole for Blade Cooling, *ARPN J. Eng. Appl. Sci.*, 2017, **12**(22), 6397–6406, DOI: 10.1039/b000000x.

23 X. H. Li and M. Antonietti, Polycondensation of Boron- and Nitrogen-Codoped Holey Graphene Monoliths from Molecules: Carbocatalysts for Selective Oxidation, *Angew. Chem., Int. Ed.*, 2013, **52**(17), 4572–4576, DOI: 10.1002/anie.201209320.

24 M. Park, Y. J. Jung, J. Kim, H. I. Lee and J. Cho, Synergistic Effect of Carbon Nanofiber/Nanotube Composite Catalyst on Carbon Felt Electrode for High-Performance All-Vanadium Redox Flow Battery, *Nano Lett.*, 2013, **13**(10), 4833–4839, DOI: 10.1021/nl402566s.

25 D. Ji, L. Fan, L. Li, N. Mao, X. Qin, S. Peng and S. Ramakrishna, Hierarchical Catalytic Electrodes of Cobalt-Embedded Carbon Nanotube/Carbon Flakes Array for Flexible Solid-State Zinc-Air Batteries Hierarchical Catalytic Electrodes of Cobalt-Embedded Carbon Nanotube/Carbon Fl Akes Array for Flexible Solid-State Zi, *Carbon*, 2019, **142**, 379–387, DOI: 10.1016/j.carbon.2018.10.064.

26 S. Li, Y. Luo, W. Lv, W. Yu, S. Wu and P. Hou, Vertically Aligned Carbon Nanotubes Grown on Graphene Paper as Electrodes in Lithium-Ion Batteries and Dye-Sensitized Solar Cells, *Adv. Energy Mater.*, 2011, **1**, 486–490, DOI: 10.1002/aenm.201100001.

27 D. Ji, S. Peng, D. Safanama, H. Yu, L. Li, G. Yang, X. Qin, M. Srinivasan, S. Adams and S. Ramakrishna, Design of 3-Dimensional Hierarchical Architectures of Carbon and Highly Active Transition Metals (Fe, Co, Ni) as Bifunctional Oxygen Catalysts for Hybrid Lithium-Air Batteries, *Chem. Mater.*, 2017, **29**(4), 1665–1675, DOI: 10.1021/acs.chemmater.6b05056.

28 Y. Chen, X. Li, K. Park, J. Song, J. Hong, L. Zhou, Y. W. Mai, H. Huang and J. B. Goodenough, Hollow Carbon-Nanotube/Carbon-Nanofiber Hybrid Anodes for Li-Ion Batteries, *J. Am. Chem. Soc.*, 2013, **135**(44), 16280–16283, DOI: 10.1021/ja408421n.

29 J. Zhou, J. Chen, S. Han, H. Zhao, J. Bai, Z. Yang, X. Mu, Y. Liu, D. Bian, G. Sun, *et al.*, Constructing Optimized Three-Dimensional Electrochemical Interface in Carbon Nanofiber/Carbon Nanotube Hierarchical Composites for High-Energy-Density Supercapacitors, *Carbon*, 2017, **111**, 502–512, DOI: 10.1016/j.carbon.2016.10.036.

30 N. Li, D. K. Bediako, R. G. Hadt, D. Hayes, T. J. Kempa, F. Von Cube, D. C. Bell, L. X. Chen and D. G. Nocera, Influence of Iron Doping on Tetravalent Nickel Content in Catalytic Oxygen Evolving Films, *Proc. Natl. Acad. Sci. U. S. A.*, 2017, **114**(7), 1486–1491, DOI: 10.1073/pnas.1620787114.

31 J. Deng, P. Ren, D. Deng, L. Yu, F. Yang and X. Bao, Highly Active and Durable Non-Precious-Metal Catalysts Encapsulated in Carbon Nanotubes for Hydrogen Evolution Reaction, *Energy Environ. Sci.*, 2014, **7**(6), 1919–1923, DOI: 10.1039/c4ee00370e.

32 S. Ci, S. Mao, Y. Hou, S. Cui, H. Kim, R. Ren, Z. Wen and J. Chen, Rational Design of Mesoporous NiFe-Alloy-Based Hybrids for Oxygen Conversion Electrocatalysis, *J. Mater. Chem. A*, 2015, **3**(15), 7986–7993, DOI: 10.1039/c5ta00894h.

33 C. Hu, L. Wang, Y. Zhao, M. Ye, Q. Chen, Z. Feng and L. Qu, Designing Nitrogen-Enriched Echinus-like Carbon Capsules for Highly Efficient Oxygen Reduction Reaction and Lithium Ion Storage, *Nanoscale*, 2014, **6**(14), 8002–8009, DOI: 10.1039/c4nr01184h.

34 S. Gupta, L. Qiao, S. Zhao, H. Xu, Y. Lin, S. V. Devaguptapu, X. Wang, M. T. Swihart and G. Wu, Highly Active and Stable Graphene Tubes Decorated with FeCoNi Alloy Nanoparticles *via* a Template-Free Graphitization for Bifunctional Oxygen Reduction and Evolution, *Adv. Energy Mater.*, 2016, **6**(22), 1–12, DOI: 10.1002/aenm.201601198.

35 S. M. Unni, R. Illathvalappil, S. N. Bhange, H. Puthenpediakkal and S. Kurungot, Carbon Nanohorn-Derived Graphene Nanotubes as a Platinum-Free Fuel Cell Cathode, *ACS Appl. Mater. Interfaces*, 2015, **7**(43), 24256–24264, DOI: 10.1021/acsami.5b07802.

36 Z. Wang, M. Li, L. Fan, J. Han and Y. Xiong, Fe/Ni-N-CNFs Electrochemical Catalyst for Oxygen Reduction Reaction/Oxygen Evolution Reaction in Alkaline Media, *Appl. Surf. Sci.*, 2017, **401**, 89–99, DOI: 10.1016/j.apsusc.2016.12.242.

37 Z. Liu, H. Yu, B.-X. Dong, X. Yu and L. Feng, Electrochemical Oxygen Evolution Reaction Efficiently Boosted by Thermal-Driving Core-Shell Structure Formation in Nanostructured

FeNi/S, N-Doped Carbon Hybrid Catalyst, *Nanoscale*, 2018, **10**(35), 16911–16918.

38 T. Palaniselvam, B. P. Biswal and R. Banerjee, Zeolitic Imidazolate Framework (ZIF)-Derived, Hollow-Core, Nitrogen-Doped Carbon Nanostructures for Oxygen-Reduction Reactions in PEFCs, *Chem.–Eur. J.*, 2013, **19**(28), 9335–9342, DOI: 10.1002/chem.201300145.

39 G. Wu, M. Nelson, S. Ma, H. Meng, G. Cui and P. K. Shen, Synthesis of Nitrogen-Doped Onion-like Carbon and Its Use in Carbon-Based CoFe Binary Non-Precious-Metal Catalysts for Oxygen-Reduction, *Carbon*, 2011, **49**(12), 3972–3982, DOI: 10.1016/j.carbon.2011.05.036.

40 Y. Fan, Z. Zhao, Q. Zhou, G. Li and X. Wang, Nitrogen-Doped Carbon Microfibers with Porous Textures, *Carbon*, 2013, **58**, 128–133, DOI: 10.1016/j.carbon.2013.02.040.

41 H. Liu, Y. Zhang, R. Li, X. Sun, S. Désilets, H. Abou-Rachid, M. Jaidann and L. S. Lussier, Structural and Morphological Control of Aligned Nitrogen-Doped Carbon Nanotubes, *Carbon*, 2010, **48**(5), 1498–1507, DOI: 10.1016/j.carbon.2009.12.045.

42 J. Liu, Y. Zhang, M. I. Ionescu, R. Li and X. Sun, Nitrogen-Doped Carbon Nanotubes with Tunable Structure and High Yield Produced by Ultrasonic Spray Pyrolysis, *Appl. Surf. Sci.*, 2011, **257**(17), 7837–7844, DOI: 10.1016/j.apsusc.2011.04.041.

43 X. Wang, Q. Li, H. Pan, Y. Lin, Y. Ke, H. Sheng, M. T. Swihart and G. Wu, Size-Controlled Large-Diameter and Few-Walled Carbon Nanotube Catalysts for Oxygen Reduction, *Nanoscale*, 2015, **7**(47), 20290–20298, DOI: 10.1039/c5nr05864c.

44 A. C. Ferrari and J. Robertson, Interpretation of Raman Spectra of Disordered and Amorphous Carbon, *Phys. Rev. B: Condens. Matter Mater. Phys.*, 2000, **61**(20), 95–107.

45 M. S. Dresselhaus, A. Jorio, A. G. Souza Filho and R. Saito, Defect Characterization in Graphene and Carbon Nanotubes Using Raman Spectroscopy, *Philos. Trans. R. Soc., A*, 2010, **368**(1932), 5355–5377, DOI: 10.1098/rsta.2010.0213.

46 M. Li, X. Bo, Y. Zhang, C. Han, A. Nsabimana and L. Guo, Cobalt and Nitrogen co-Embedded Onion-like Mesoporous Carbon Vesicles as Efficient Catalysts for Oxygen Reduction Reaction, *J. Mater. Chem. A*, 2014, **2**(30), 11672–11682, DOI: 10.1039/c4ta01078g.

47 R. Schönfelder, F. Avilés, M. Knupfer, M. H. Rümmeli, F. Avilés and M. Knupfer, Influence of Architecture on the Raman Spectra of Acid-Treated Carbon Nanostructures, *J. Exp. Nanosci.*, 2014, **9**(9), 931–941, DOI: 10.1080/17458080.2012.750763.

48 J. Liang, X. Du, C. Gibson, X. W. Du and S. Z. Qiao, N-Doped Graphene Natively Grown on Hierarchical Ordered Porous Carbon for Enhanced Oxygen Reduction, *Adv. Mater.*, 2013, **25**(43), 6226–6231, DOI: 10.1002/adma.201302569.

49 K. S. W. Sing, D. H. Everett, R. A. W. Haul, L. Moscou, R. S. Pierotti, J. Rouquerol and T. Siemieniewska, Reporting Physisorption Data for Gas/Solid Systems with Special Reference to the Determination of Surface Area and Porosity, *Pure Appl. Chem.*, 1985, **57**(4), 603–619, DOI: 10.1351/pac198557040603.

50 Y. Zhang, Z. Sun, H. Wang, Y. Wang, M. Liang and S. Xue, Nitrogen-Doped Graphene as a Cathode Material for Dye-Sensitized Solar Cells: Effects of Hydrothermal Reaction and Annealing on Electrocatalytic Performance, *RSC Adv.*, 2015, **5**, 10430–10439, DOI: 10.1039/C4RA13224F.

51 A. Kong, X. Zhu, Z. Han, Y. Yu, Y. Zhang, B. Dong and Y. Shan, Ordered Hierarchically Micro- and Mesoporous Fe–N_x-Embedded Graphitic Architectures as Efficient Electrocatalysts for Oxygen Reduction Reaction, *ACS Catal.*, 2014, **4**(6), 1793–1800, DOI: 10.1021/cs401257j.

52 S. Piontek, C. Andronescu, A. Zaichenko, B. Konkena, K. Puring, B. Marler, H. Antoni, I. Sinev, M. Muhler, D. Mollenhauer, *et al.*, Influence of the Fe:Ni Ratio and Reaction Temperature on the Efficiency of $(Fe_xNi_{1-x})_9S_8$ Electrocatalysts Applied in the Hydrogen Evolution Reaction, *ACS Catal.*, 2018, **8**, 987–996, DOI: 10.1021/acscatal.7b02617.

53 Z. Zhao, H. Wu, H. He, X. Xu and Y. Jin, Self-Standing Non-Noble Metal (Ni-Fe) Oxide Nanotube Array Anode Catalysts with Synergistic Reactivity for High-Performance Water Oxidation, *J. Mater. Chem. A*, 2015, **3**(13), 7179–7186, DOI: 10.1039/C5TA00160A.

54 J. Lee, G. S. Park, S. T. Kim, M. Liu and J. Cho, A Highly Efficient Electrocatalyst for the Oxygen Reduction Reaction: N-Doped Ketjenblack Incorporated into Fe/Fe_3C-Functionalized Melamine Foam, *Angew. Chem., Int. Ed.*, 2013, **52**(3), 1026–1030, DOI: 10.1002/anie.201207193.

55 H. Wu, J. Geng, H. Ge, Z. Guo, Y. Wang and G. Zheng, Egg-Derived Mesoporous Carbon Microspheres as Bifunctional Oxygen Evolution and Oxygen Reduction Electrocatalysts, *Adv. Energy Mater.*, 2016, **6**(20), 1600794, DOI: 10.1002/aenm.201600794.

56 Z. Lin, G. Waller, Y. Liu, M. Liu and C. Wong, Facile Synthesis of Nitrogen-Doped Graphene via Pyrolysis of Graphene Oxide and Urea, and Its Electrocatalytic Activity toward the Oxygen-Reduction Reaction, *Adv. Energy Mater.*, 2012, **2**, 884–888, DOI: 10.1002/aenm.201200038.

57 J. Ren, M. Antonietti and T. Fellinger, Efficient Water Splitting Using a Simple Ni/N/C Paper Electrocatalyst, *Adv. Energy Mater.*, 2014, **5**(6), 1–6, DOI: 10.1002/aenm.201401660.

58 Y. Yuan, L. Yang, B. He, E. Pervaiz, Z. Shao and M. Yang, Cobalt-Zinc Nitride on Nitrogen Doped Carbon Black Nanohybrids as a Non-Noble Metal Electrocatalyst for Oxygen Reduction Reaction, *Nanoscale*, 2017, **9**, 6259–6263, DOI: 10.1039/C7NR02264F.

59 Q. Lai, Q. Su, Q. Gao, Y. Liang, Y. Wang and Z. Yang, In Situ Self-Sacrificed Template Synthesis of Fe-N/G Catalysts for Enhanced Oxygen Reduction, *ACS Appl. Mater. Interfaces*, 2015, **7**(32), 18170–18178.

60 Z. Xing, Z. Ju, Y. Zhao, J. Wan, Y. Zhu, Y. Qiang and Y. Qian, One-Pot Hydrothermal Synthesis of Nitrogen-Doped Graphene as High-Performance Anode Materials for Lithium Ion Batteries, *Sci. Rep.*, 2016, **6**, 1–10, DOI: 10.1038/srep26146.

61 V. Datsyuk and K. Papagelis, Chemical Oxidation of Multi-Walled Carbon Nanotubes, *Carbon*, 2008, **46**, 833–840, DOI: 10.1016/j.carbon.2008.02.012.

62 J. S. Lee, G. S. Park, S. T. Kim, M. Liu and J. Cho, A Highly Efficient Electrocatalyst for the Oxygen Reduction Reaction: N-Doped Ketjenblack Incorporated into Fe/Fe$_3$C-Functionalized Melamine Foam, *Angew. Chem., Int. Ed.*, 2013, **52**(3), 1026–1030, DOI: 10.1002/anie.201207193.

63 M. Liu and W. Chen, Green Synthesis of Silver Nanoclusters Supported on Carbon Nanodots: Enhanced Photoluminescence and High Catalytic Activity for Oxygen Reduction Reaction, *Nanoscale*, 2013, **5**(24), 12558–12564, DOI: 10.1039/c3nr04054b.

64 H. Oh, J. Oh, W. Hee, H. Kim and H. Kim, The Influence of the Structural Properties of Carbon on the Oxygen Reduction Reaction of Nitrogen Modified Carbon Based Catalysts, *Int. J. Hydrogen Energy*, 2011, **36**(14), 8181–8186, DOI: 10.1016/j.ijhydene.2011.04.139.

65 L. Lai, J. R. Potts, D. Zhan, L. Wang, K. Poh, C. Tang and H. Gong, Exploration of the Active Center Structure of Nitrogen-Doped Graphene-Based Catalysts for Oxygen Reduction Reaction, *Energy Environ. Sci.*, 2012, **5**(7), 7936–7942, DOI: 10.1039/c2ee21802j.

66 G. Tuci, C. Za, P. D. Ambrosio, S. Caporali, M. Ceppatelli, A. Rossin, T. Tsou, M. Innocenti and G. Giambastiani, Tailoring Carbon Nanotube N-Dopants While Designing Metal-Free Electrocatalysts for the Oxygen Reduction Reaction in Alkaline Medium, *ACS Catal.*, 2013, **3**, 2108–2111, DOI: 10.1021/cs400379h.

67 S. Ni, Z. Li and J. Yang, Oxygen Molecule Dissociation on Carbon Nanostructures with Different Types of Nitrogen Doping, *Nanoscale*, 2012, **4**(4), 1184–1189, DOI: 10.1039/c1nr11086a.

68 J. Masa, W. Xia, M. Muhler and W. Schuhmann, On the Role of Metals in Nitrogen-Doped Carbon Electrocatalysts for Oxygen Reduction, *Angew. Chem., Int. Ed.*, 2015, **54**(35), 10102–10120, DOI: 10.1002/anie.201500569.

69 J. Wang and F. Ciucci, Boosting Bifunctional Oxygen Electrolysis for N-Doped Carbon via Bimetal Addition, *Small*, 2017, **13**(16), 1–15, DOI: 10.1002/smll.201604103.

70 M. Pumera and H. Iwai, Metallic Impurities within Residual Catalyst Metallic Nanoparticles Are in Some Cases Responsible for "Electrocatalytic" Effect of Carbon Nanotubes, *Chem.–Asian J.*, 2009, **4**(4), 554–560, DOI: 10.1002/asia.200800420.

71 H. Wu, M. Zeng, Z. Li, X. Zhu, C. Tian, X. Chungu, L. He and S. Dai, Coupling FeNi Alloys and Hollow Nitrogen-Enriched Carbon Framework Leads to High-Performance Oxygen Electrocatalysis for Rechargeable Zinc-Air Battery, *Sustainable Energy Fuels*, 2019, **3**(1), 136–141, DOI: 10.1039/C8SE00362A.

72 Y. Yan, J. Miao, Z. Yang, F.-X. Xiao, H. B. Yang, B. Liu and Y. Yang, Carbon Nanotube Catalysts: Recent Advances in Synthesis, Characterization and Applications, *Chem. Soc. Rev.*, 2015, **44**(10), 3295–3346, DOI: 10.1039/C4CS00492B.

73 Z. Liu, H. Yu, B. Dong, X. Yua and L. Fen, Electrochemical Oxygen Evolution Reaction Efficiently Boosted by Thermal-Driving Core-Shell Structure Formation in Nanostructured FeNi/S, N-Doped Carbon Hybrid Catalyst, *Nanoscale*, 2018, **10**(35), 16911–16918, DOI: 10.1039/C8NR05587D.